J Appl Electrochem (2010) 40:943–954
DOI 10.1007/s10800-010-0099-5

ORIGINAL PAPER

SOFC fuelled by methane without coking: optimization of electrochemical performance

J. M. Klein · S. Georges · Y. Bultel

Received: 1 December 2008 / Accepted: 25 January 2010 / Published online: 16 February 2010

Abstract In recent years, fuel cell technology has attracted considerable attention from several fields of scientific research as fuel cells produce electric energy with high efficiency, emit little noise, and are non-polluting. Solid oxide fuel cells (SOFCs) are particularly important for stationary applications due to their high operating temperature (1,073–1,273 K). Methane appears to be a fuel of great interest for SOFC systems because it can be directly converted into hydrogen by direct internal reforming (DIR) within the SOFC anode. Unfortunately, internal steam reforming in SOFC leads to inhomogeneous temperature distributions which can result in mechanical failure of the cermet anode. Moreover this concept requires a large amount of steam in the fed gas. To avoid these problems, gradual internal reforming (GIR) can be used. GIR is based on local coupling between steam reforming and hydrogen oxidation. The steam required for the reforming reaction is obtained by the hydrogen oxidation. However, with GIR, Boudouard and cracking reactions can involve a risk of carbon formation. To cope with carbon formation a new cell configuration of SOFC electrolyte support was studied. This configuration combined a catalyst layer (0.1%Ir–CeO_2) with a classical anode, allowing GIR without coking. In order to optimise the process a SOFC model has been developed, using the CFD-Ace+ software package, and including a thin electrolyte. The impact of a thin electrolyte on previous conclusions has been assessed. As predicted, electrochemical performances are higher and carbon formation is always avoided. However a sharp decrease in the electrochemical performances appears at high current densities due to steam clogging.

Keywords SOFC · Gradual internal reforming · Simulation · CFD-Ace+

List of symbols

D_i	Diffusion coefficient of the i-th species ($m^2\ s^{-1}$)
$D_{i,\text{eff}}$	Effective diffusion coefficient of the i-th species ($m^2\ s^{-1}$)
E_0	Voltage between the electrolyte and the nickel at equilibrium (V)
F	Faraday constant (96500) (C mol^{-1})
J_i	Diffusion flux of the i-th species (mol $m^{-2}\ s^{-1}$)
K_{E1}	Equilibrium constant of steam methane reforming reaction (Pa^2)
K_{E2}	Equilibrium constant of water gas shift reaction (–)
K_{B}	Equilibrium constant of Boudouard reaction (Pa^{-1})
K_{C}	Equilibrium constant of Cracking reaction (Pa)
M	Molecular weight of the mixture of gases (kg $kmol^{-1}$)
P_i	Partial pressure of the i-th species (Pa)
R	Universal gas constant (8.314) (J $mol^{-1}\ K^{-1}$)
$(S/V)_{\text{eff}}$	Effective surface-to-volume ratio ($m^2\ m^{-3}$)
T	Temperature (K)
a_c	Carbon activity (–)
d_{pore}	Pore diameter (M)
H	Gas mixture enthalpy (J kg^{-1})
h_{B}	Solid-phase enthalpy (J kg^{-1})
i	Current density (A m^{-2})
$[i]$	Molar concentration of the i-th species (kmol m^{-3})

J. M. Klein · S. Georges · Y. Bultel (✉)
Laboratoire d'Electrochimie et de Physico-Chimie des Matériaux et des Interfaces (LEPMI), UMR 5631
CNRS-GINP-UJF, BP 75, 38402 Saint Martin d'Hères, France
e-mail: yann.bultel@lepmi.grenoble-inp.fr

$[i]_0$	Reference concentration of the i-th species (kmol m^{-3})
j_{a0}	Exchange current density of the anode (A m^{-2})
j_{at}	Faradaic current due to anodic reaction (A m^{-2})
j_{ct}	Faradaic current due to cathodic reaction (A m^{-2})
P	Total pressure (Pa)
Q	Heat flux (W m^{-2})
r_k	Reaction rate of the k-th reaction (Kmol m^{-3} s^{-1})
U_{cell}	Cell potential (V)
v	Fluid velocity (m s^{-1})
w_i	Mass fraction of the i-th species (–)
x_i	Molar fraction of the i-th species (–)

Greeks

α	Boudouard coefficient (–)
α_a	Anodic Tafel constant (–)
α_c	Cathodic Tafel constant (–)
β	Cracking coefficient (–)
δ	Shear stress tensor (–)
ε	Porosity (–)
ϕ_{as}	Ionic phase potential at anode (V)
ϕ_{aM}	Electronic phase potential at anode (V)
ϕ_{es}	Ionic phase potential of the electrolyte (V)
γ	Boudouard + Cracking coefficient (–)
λ_B	Thermal conductivity of the solid phase (W m^{-1} K^{-1})
η_a	Anode overpotential (V)
κ	Permeability (m^2)
μ	Dynamic viscosity of the gas mixture (Pa s)
μ_i	Dynamic viscosity of the i-th species (Pa s)
ρ	Mass density of the gas mixture (kg m^{-3})
σ_{as}	Ionic phase conductivity at anode (Ω^{-1} m^{-1})
σ_{aM}	Electronic phase conductivity at anode (Ω^{-1} m^{-1})
σ_{es}	Ionic phase conductivity of the electrolyte (Ω^{-1} m^{-1})
τ	Tortuosity of pores (m m^{-1})

1 Introduction

Solid oxide fuel cells (SOFCs) are promising candidates for power generation while preserving the environment. SOFCs can nowadays operate with good efficiency and decent durability with hydrogen as the fuel at intermediate temperature (873–973 K), even though technological efforts still have to be made in order to increase life time and reduce fabrication, operation and recycling costs. Given the actual energy context, and in particular the aspects concerning production, storage and distribution infrastructures of hydrogen, the use of other fuels based on hydrocarbons sounds interesting to be considered in the next decades. Natural gas, bio-gas, waste fuels, bio-ethanol or other sources are interesting candidates for clean and cheap operation of various devices like SOFC, instead of oil-based fuels. In this context, several solutions have been proposed to overcome technical issues and enable direct and stable hydrocarbon operation of SOFC without coke formation [1]. The concept of gradual internal reforming (GIR) [2] with the addition of a catalyst layer onto the conventional Ni–YSZ cermet anode is one of them. The lack of coking at the Ni-based anode can be explained by the fact that the greater part of the reforming reaction occurs in the catalyst layer and therefore most of the hydrocarbon species are eliminated before the fuel reaches the anode. A key element of this strategy was the choice of a catalyst material that promotes hydrocarbon reforming but does not itself cause coking.

Gradual internal reforming is based on local coupling between steam reforming of the fuel, which occurs on a catalyst (nickel for a Ni–YSZ cermet anode) and hydrogen electrochemical oxidation, which occurs at the electrode/electrolyte/gas three phase boundary. GIR also enables the hydrogen required by the electrochemical reaction to be generated in situ. However, in contrast to direct internal reforming (DIR) where the steam is fed in a consequent way, this process requires a very weak inlet steam contribution. Indeed the steam used by the reforming reaction is produced by the electrochemical reaction all along the cell. This approach is based on the works of Vernoux et al. [2], Georges et al. [3] and Klein et al. [4] who have studied the feasibility of GIR in SOFCs.

A previous work [5], using the CFD-Ace+ software package, proposed a model of gas diffusion electrode to simulate the behavior of a SOFC under conditions of GIR with the addition of a catalyst layer. A conventional anode material (Ni–YSZ cermet) designed to operate with high H_2O/CH_4 ratios was covered with a catalytic layer active for methane reforming and resistant to carbon formation. This concept, close to the one mentioned by Barnett and co-workers [6], was referred as electro-catalytic dissociation. A realistic three phase boundary distribution was considered through the porous electrode thickness. The electrochemical reactions within the porous electrodes described using the Butler–Volmer equations at the three phase boundary. Modeling was based on solving the conservation equations of mass, momentum, energy, species and electric current by using a finite volume approach on 2D grids of arbitrary topology. Simulations with the CFD-Ace+ software package allowed the calculation of the distributions of partial pressures (CH_4, H_2, CO, CO_2, and H_2O), current density and potentials of electronic and ionic phases within the anode part (i.e. gas channel and cermet anode), and finally the calculation of the thermal gradient in the cell. It was demonstrated that GIR of methane, using

pure methane and in the presence of small quantities of steam, can be achieved without any carbon deposition (of a thermodynamic nature) using this original geometry. With a catalyst layer thickness of 900 μm and a kinetic reforming rate 10 times higher than the reforming rate in the cermet, carbon deposition is not thermodynamically favoured throughout the length of the tubular SOFC.

Catalytic tests [7] have been done and it has been proved that iridium impregnated ceria is a promising candidate for the catalytic layer. Based on this work and on previous simulations, an electrolyte support SOFC cell has been designed. The article of Klein et al. [8] presents the associated results. The cell associated a good anode material (Ni/YSZ cermet) and a catalyst layer (Ir/CeO_2) deposited on a thick YSZ electrolyte. It was operated under GIR conditions in dry methane. Stable operation without steam at the anode inlet was obtained for several hours, demonstrating the efficiency of the GIR concept together with high CH_4 conversion and anode protection by the highly active catalyst layer. Electro-catalytic dissociation associated with GIR allows stable operation in dry methane without coking in the anode layer. The cell had to be optimized to increase the power density and reduce the operation temperature.

Due to the experimental equipment the cell has been designed with a thick electrolyte. One way to optimize the cell performances is thus to reduce the thickness of the YSZ electrolyte in order to reduce ionic ohmic losses in the electrolyte. The aim of this study is to compare the case of the electrolyte-supported system to a metal-supported cell with a thin electrolyte. This study proposes also a model of SOFC which takes into account the kinetics of the reforming reaction on the Ir/CeO_2 catalyst in order to assess the limitations under current of the precedent design. The influence on the carbon deposition of the real kinetic in the catalyst layer is thus studied, based on thermodynamic considerations.

2 Tubular SOFC model descriptions

2.1 Description of the tubular SOFC

An SOFC is an assembly of an electrolyte sandwiched between anode and cathode electrodes [4]. The SOFC length in the present modeling is 30 mm and the thicknesses of the different parts of the SOFC are given in Table 1. Both, an electrolyte-supported (thick electrolyte = 1 mm) and a metal-supported (thin electrolyte = 50 μm) geometry are considered for this model. The presented modelling concerns only the region near the inlet of a real SOFC where the risk of carbon deposition is very important.

Table 1 Geometrical parameters of the tubular SOFC (thick electrolyte/thin electrolyte)

Geometry	Inner radius (mm)	Outer radius (mm)
Fuel channel	3.4/2.45	4.4/3.45
Catalyst layer	2.4/1.45	3.4/2.45
Collector	2.3/1.35	2.4/1.45
Anode	2.2/1.25	2.3/1.35
Electrolyte	1.2/1.2	2.2/1.25
Cathode	1.1/1.1	1.2/1.2
Collector	1.0/1.0	1.1/1.1
Air channel	0	1.0/1.0

In the present model, mass and charge transport phenomena coupled with chemical and electrochemical reactions are investigated within the inlet of the SOFC as described in Fig. 1. A finite volume method using a computational grid allows solving the mass, charge, energy, momentum balances including transport through porous media and chemical and electrochemical reactions within porous electrodes in a gas diffusion electrode model. The set of resulting conservation equations is solved using the commercial software package CFD-Ace+ [9].

This model deals with a two-dimension geometry at steady state conditions for a SOFC. The O_2/N_2 (air) and CH_4/H_2O mixtures are supplied at the cathode and at the anode gas channel, respectively. Fuel consumption at the anode results from both internal reforming and water gas shift reactions. Fuel composition can include any combination of methane and steam.

In the gas phase, the mass conservation equation is described as follows:

$$\nabla \cdot (\varepsilon \rho \mathbf{v}) = 0 \tag{1}$$

where ε is the porosity of the medium, defined as the ratio of the volume occupied by the pores to the total volume of the porous medium, ρ is the density and $\mathbf{v}$ is the velocity vector of the gas mixture.

The momentum conservation equation, when compressibility and turbulence effects are not taken into account, is described by Klein et al. [4]:

$$\nabla \cdot (\varepsilon \rho \mathbf{v} \cdot \mathbf{v}) = -\varepsilon \nabla p + \nabla \cdot (\varepsilon \boldsymbol{\delta}) + \frac{\varepsilon^2 \mu \mathbf{v}}{\kappa} \tag{2}$$

where p and $\mathbf{v}$ are the pressure and the velocity vector of the gas mixture, $\boldsymbol{\delta}$ is the shear tress tensor and μ is the dynamic viscosity of the fluid. ρ and μ are properties are dependent on temperature. κ is the permeability which is a quantity representing the square of the effective volume to surface area ratio of the porous matrix. The last term in Eq. 2 represents the Darcy's drag force imposed by the pore walls on the fluid within the pores, and usually results in a significant pressure drop across the porous medium.

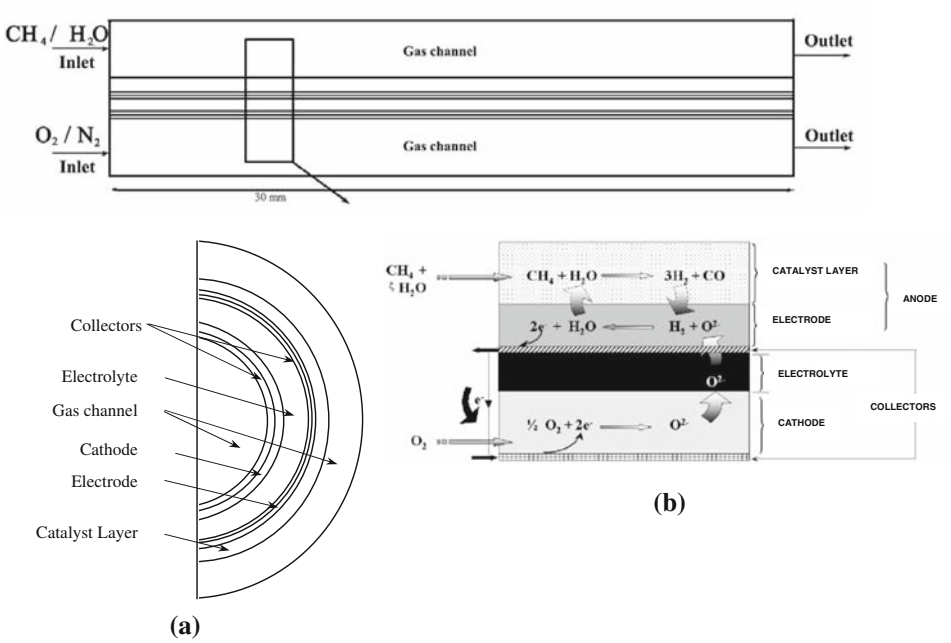

Fig. 1 Geometry of the tubular SOFC cell. **a** Cross section of the tubular SOFC; **b** zoom

The conservation equation for energy (Eq. 3) may be expressed as [9–11]:

$$\nabla \cdot (\varepsilon \rho \mathbf{v} h) = \nabla \cdot \mathbf{q} + \varepsilon \boldsymbol{\delta} \cdot \nabla \mathbf{v} + \varepsilon \frac{\mathrm{d}p}{\mathrm{d}t} - j_t \left(\frac{S}{V}\right)_{\mathrm{eff}} (\phi_{\mathrm{aM}} - \phi_{\mathrm{aS}}) + \frac{|\mathbf{i} \cdot \mathbf{i}|}{\sigma} \quad (3)$$

where h is the gas mixture enthalpy; h_{B} and ρ_{B} are, respectively, the solid phase enthalpy and density. The heat flux, $\mathbf{q}$, is comprised of contributions due to thermal conduction and species diffusion (Eq. 4), and is written as:

$$\mathbf{q} = \lambda \nabla T + \sum_i \mathbf{J}_i h_i \quad (4)$$

h_i being species i enthalpies (defined here as sum of enthalpy of formation and latent heat, in case of phase change), $\mathbf{J}_i$ their diffusion fluxes, and T the temperature. The thermal conductivity, λ, of the porous medium is an effective thermal conductivity of the fluid and solid regions taken together [4]. The last two terms in Eq. 3 represent electrical work and Joule heating, respectively. The irreversible losses due to the reaction (conversion of chemical energy to heat energy) manifest themselves automatically through the second term on the right hand side of Eq. 4 because the definition of enthalpy includes both the enthalpy of formation and the sensible enthalpy.

The cell walls are considered adiabatic. The conservation equation for energy (Eq. 3) is solved in each volume element and a continuity condition is imposed at interfaces. Then the specific heat transfer coefficients are calculated by the classical Jannaf method. Knowing the enthalpy and the heat transfer coefficients it is thus possible to assess the temperature distributions. However the heat transfer by radiation is not taken into account here because of the weakness of the temperature gradient in the cell.

The mass and charge balances are numerically solved with the following boundary conditions: Potentials are set to zero for the anodic collector and to an input value for the cathodic one. It is worth mentioning that no internal boundary conditions are imposed when using the CFD software package. The ionic current is assumed to be zero on the surface of both collectors but variable elsewhere. Electronic ohmic drops along the gas channel can be neglected because of the high electronic conductivity assumed for the electronic conductor.

2.2 Anode

The anode material is a composite between nickel and yttria-stabilized zirconia (Ni–YSZ cermet). The anode is considered in modeling as a porous gas diffusion electrode wherein the electrochemical reaction occurs at the triple phase boundary, i.e. at the interface between the electronic conductor (nickel), the ionic conductor (YSZ) and the gas phase (fuel). Current density (related to charge transports) is thus the sum of two inseparable but different contributions: one related to ionic species and the other to electrons transport. Mass transport occurs within the gas pores and charge transport phenomena depend on four electric parameters: ionic and electronic conductivities σ_{as}, σ_{aM} (S m^{-1}) and potentials ϕ_{as} and ϕ_{aM} (V).

The GIR consists of adding the function of reformer to the SOFC anode, a direct production of hydrogen from methane being possible due to the high temperature in the fuel cell. Figure 1 presents the principle of GIR coupled

with electro-catalytic dissociation [8]. To avoid cracking by contact with methane, anodic current collection cannot be made with conventional grids pressed onto the anode because of the addition of the catalyst layer. SOFC cell modelling was performed considering that current collectors had to be placed between the electrolyte and the anode.

Methane can thus be converted into H_2 and CO by heterogeneous steam reforming (5) and heterogeneous water gas shift (6):

$$CH_4 + H_2O \leftrightarrow CO + 3H_2 \tag{5}$$

$$CO + H_2O \leftrightarrow CO_2 + H_2 \tag{6}$$

while hydrogen is electrochemically oxidized within the anode (7):

$$\frac{1}{2}H_2 + \frac{1}{2}O^{2-} \rightarrow \frac{1}{2}H_2O + e^- \tag{7}$$

There has been a number of papers published with information on the kinetics of methane steam reforming on nickel-based anode materials [12–17]. These studies of the kinetics of methane steam reforming reaction were carried out with the catalysts of different compositions prepared by various methods and of different particle size, and over wide ranges of temperature and pressure. Therefore, there were suggested many different mechanisms and kinetic models suggested. However, it is impossible to develop generalized kinetic models, which can be applied to different catalyst with only a change in parameter to suit to each catalyst [16]. The kinetics model for methane steam reforming over nickel-based catalysts developed by Xu and Froment [12] is the most general expression. The rate expressions of the steam reforming reaction (5) and water gas shift (6) used for simulation were determined experimentally by Lehnert et al. [13, 14]. These kinetic models give a reasonable representation of the experimental data obtained on Ni/YSZ cermet. They differ partly from the one proposed by Xu and Froment [12]. The volumetric reaction rate of the methane steam reforming reaction (mol m^{-3} s^{-1}), expressed as moles of methane reacted per unit volume and time [14] can be written as:

$$r_{E1} = k_{E1}^{+}[CH_4][H_2O] - k_{E1}^{-}[H_2]^3[CO] \tag{8}$$

where k_{E1}^{+} and k_{E1}^{-} denote the velocity constant of forward and backward reaction and $[i]$ the concentration of gas species i (mol m^{-3}). The volumetric rate of the water shift reaction (mol m^{-3} s^{-1}) can be similarly formulated with the velocity constants k_{E2}^{+} and k_{E2}^{-} as:

$$r_{E2} = k_{E2}^{+}[CO][H_2O] - k_{E2}^{-}[H_2][CO_2] \tag{9}$$

At the operating temperature range of 800–1,000 °C, it can be assumed that the water gas shift reaction is very quick and remains near equilibrium [4].

These volumetric reaction rates can be rewritten by considering the equilibrium constants [12, 17] for methane steam reforming and water gas shift reactions as:

$$r_{E1} = k_{E1}^{+}\left([CH_4][H_2O] - \frac{[H_2]^3[CO]}{K_{E1}}\right) \tag{10}$$

$$r_{E2} = k_{E2}^{+}\left([CO][H_2O] - \frac{[H_2][CO_2]}{K_{E2}}\right) \tag{11}$$

where K_{Ei} are the equilibrium constants of the reactions (5) and (6).

Finally the kinetics of electrochemical reaction (7) within the porous electrode can be described using the Butler–Volmer equation at the triple phase boundary [18]:

$$j_{at} = j_{a0}\left(\exp\left(\frac{\alpha_a F}{RT}\eta_a\right)\frac{[H_2]}{[H_2]_0} - \exp\left(-\frac{\alpha_c F}{RT}\eta_a\right)\frac{[H_2O]}{[H_2O]_0}\right) \tag{10}$$

The overpotential η is defined as:

$$\eta_a = \phi_{aM} - \phi_{as} - E_{a0} \tag{11}$$

locally determined within the porous electrode through a separate solving of the equations related to electronic and ionic potentials. E_{a0} is the potential difference between the electrolyte and the nickel in equilibrium, i.e., when no current is produced.

The other parameters are the symmetry factors α_a and α_c determined from the experimental Tafel slopes, the exchange current density j_{a0} (A m^{-2}), which are presented in Table 2, the Faraday constant F and the ideal gas law constant R. $[H_2]$ and $[H_2O]$ are interfacial concentrations. Note that j_{a0} is the exchange current density at the bulk composition and $[H_2]_0$, $[H_2O]_0$ the corresponding gas phase concentrations in the bulk.

Within a porous composite electrode, current can be split into two parts: one flowing through the ionic conducting ceramic component and the other one flowing through the electronic phase. During electrochemical reactions, electrons are then either transferred from the ionic phase to the electronic one or in the opposite way. If we consider an electrochemical reaction occurring at the anode, the charge conservation may thus be expressed by the Ohm's law as:

Table 2 Kinetics electrochemical parameters [22]

	Anode	Cathode
(S/V) j_0 (A m^{-3})	10^{12}	10^{11}
α_a	2	0.6
α_c	0.7	0.7

$$\nabla \cdot (\sigma_{\mathrm{as}} \nabla \phi_{\mathrm{as}}) = -\nabla \cdot (\sigma_{\mathrm{aM}} \nabla \phi_{\mathrm{aM}}) = j_t \left(\frac{S}{V}\right)_{\mathrm{eff}} \quad (12)$$

Note that the porous electrode is treated as an effective homogeneous flooded medium characterised by an effective ionic conductivity which depends on the microstructural characteristics of the electrode [19].

On the other hand, mass balances for each gas phase species i are given at steady-state by:

$$\nabla \cdot (\varepsilon \rho \mathbf{v} w_i) = \nabla \cdot J_i + \sum_{p=1}^{3} Z_{ip} \quad (13)$$

Here the first term corresponds to convection, term Z_{ip} stands for the creation or consumption rate of species i (per unit volume of porous medium) and p represents the three reactions which take place at the same time at the anode. Thus the last term can be expressed under three forms, resulting from the anodic electrochemical reaction, the steam reforming reaction or the water gas-shift reaction on the surface of the nickel catalyst particles:

$$\left(v''_{i1} - v'_{i1}\right) r_{\mathrm{E1}} = Z_{i1} \quad (14)$$

$$\left(v''_{i2} - v'_{i2}\right) r_{\mathrm{E2}} = Z_{i2} \quad (15)$$

$$M_i \left(v''_{i3} - v'_{i3}\right) \left(\frac{S}{V}\right)_{eff} \frac{j_{at}}{F} = Z_{i3} \quad (16)$$

where v'_{i1}, v''_{i1} are, respectively, the normalized stoichiometric coefficients for reactants and products, M_i and w_i are the molecular weight and the mass fraction of species i, $(S/V)_{\mathrm{eff}}$ ($\mathrm{m^2\ m^{-3}}$) is used to take into account the effective surface-to-volume ratio which is directly related to the three phase boundary surface area per unit electrode volume (anode and cathode), and $(A/V)_{\mathrm{eff}}$ is the specific catalyst surface area per unit volume of anode which is a direct representation of catalyst loading. To summarize, we can say that the mass conservation equation of species takes into account the three reactions located at the anode side (steam reforming, water gas shift and the electrochemical reaction) at the same time.

With regard to the description of the diffusion term taken into account in the mass balance (Eq. 13), the diffusion flux is given by the Stefan–Maxwell equation:

$$\mathbf{J}_i = \rho D_{i,\mathrm{eff}} \nabla w_i + \frac{\rho w_i}{M} D_{i,\mathrm{eff}} \nabla M + \rho w_i \sum_j D_{j,\mathrm{eff}} \nabla w_j + \rho w_i \frac{\nabla M}{M} \sum_j D_{j,\mathrm{eff}} w_j \quad (17)$$

which is dependent on the mass fraction of species i (w_i), the mass fraction of all the other components of the mixture (w_j) and the molar mass of the gas mixture (M). The effective mass diffusion coefficient $D_{i,\mathrm{eff}}$ is used to take the porous medium into account in the Stefan–Maxwell diffusion and must be deduced from the free stream diffusion coefficient D_i using the so-called Bruggemann model [10, 20], depending on tortuosity τ.

$$D_{i,\mathrm{eff}} = D_i \varepsilon^{\tau} \quad (18)$$

In this case, simulations were performed with a tortuosity of 4 [21], a standard value from the literature.

Finally the description is completed by the ideal gas law:

$$\rho = \frac{\mathrm{PM}}{\mathrm{RT}} \quad (19)$$

$$M = \sum_{i=1}^{N} x_i M_i \quad (20)$$

where x_i the molar fraction of species i.

2.3 Catalyst layer

The catalyst layer is placed against the anode side of the SOFC. The lack of coking at the Ni-based anode can be explained by the fact that the greater part of the reforming reaction occurs in the catalyst layer, and therefore most of the hydrocarbon species are eliminated before the fuel has reached the cermet anode. A key element of this strategy was choosing a catalyst material that promotes hydrocarbon reforming but does not itself cause coking. Some experiments have been done and Ir/CeO_2 is such a material [7].

The chemical reactions that occur in this catalyst layer are exactly the same as in the Ni–YSZ cermet. Thus, methane is converted into H_2 and CO through the steam reforming reaction (Eq. 6) and the water gas shift (Eq. 7). The hydrogen produced then moves through the cermet. The rate expression of the steam reforming reaction (5) in the catalyst layer was determined experimentally by Klein [7] for a steam to carbon (S/C) ratio ranging from 0.1 to 0.5. The reforming kinetics (mol $\mathrm{m^{-3}\ s^{-1}}$) in the catalyst layer (Ir catalyst particles) per unit volume is given equation:

$$r_{\mathrm{E4}} = k^{+}_{\mathrm{E4}} P^{1.1}_{\mathrm{CH_4}} \quad (21)$$

with a zero order dependency with respect to steam.

Mass balances for each gas phase species i within the catalyst loading are given at steady-state by:

$$\nabla \cdot (\varepsilon \rho \mathbf{v} w_i) = \nabla \cdot \mathbf{J}_i + Z_{i2} + Z_{i4} \quad (22)$$

where Z_{i4} term stands for the creation or consumption rate of species i (per unit volume of porous medium) by the steam methane reaction in the catalyst layer:

$$\left(v''_{i1} - v'_{i1}\right) r_{\mathrm{E4}} = Z_{i4} \quad (23)$$

2.4 Cathode

Cathode consists in a porous lanthanum manganite ($LaMnO_3$) doped with YSZ solid phases. Its behavior is described in the same way as previously for the anode.

Oxygen reduction reaction occurs at cathode from the electrochemical reaction:

$$\frac{1}{4}O_2 + e^- \rightarrow \frac{1}{2}O^{2-} \tag{24}$$

The faradaic current j_{ct} at cathode is obtained from a Butler–Volmer equation:

$$j_{ct} = j_{c0}\left(\exp\left(\frac{\alpha_a F}{RT}\eta_c\right) - \exp\left(-\frac{\alpha_c F}{RT}\eta_c\right)\frac{[O_2]}{[O_2]_0}\right) \tag{25}$$

where j_{c0} is the exchange current density at the bulk composition and $[O_2]_0$ the corresponding gas phase concentration in the bulk.

2.5 Electrolyte

The electrolyte material is YSZ, which is a suitable ionic conductor at high temperature. Conditions of zero electronic current and zero electronic voltage are imposed in the electrolyte to ensure that the electrolyte is completely impermeable to electrons circulation. The electrolyte potential is thus expressed by the classical Ohm's law without any charge creation or consumption within the electrolyte:

$$\sigma_{es}\left(\frac{\partial^2\phi_{es}}{\partial x^2} + \frac{\partial^2\phi_{es}}{\partial y^2}\right) = 0 \tag{26}$$

2.6 Simulation parameters

The kinetic data used in the Butler–Volmer equations are listed in Table 2 for both anode and cathode. A quite good agreement between experimental and simulated data was obtained with these kinetic electrochemical parameters [22].

The velocity constants according to [7, 13, 14] are presented in the Table 3.

Table 4 provides a brief description of the properties for the materials currently used in the various cell components of the tubular SOFC at 1,173 K.

3 Results and discussion

The high operating temperature of SOFCs allows operation under DIR, and even under GIR conditions. With operation in GIR, a delocalisation of the steam reforming reaction along the cell can happen and, consequently yield to homogenisation of the hydrogen production and temperature along the cell. However, carbon formation becomes a serious problem in SOFC that use methane at high temperature in GIR mode. Parasitic Boudouard and cracking reactions can lead to the formation of a carbon deposit. It is worth mentioning that Boudouard and cracking reactions are not favoured in the catalytic layer but can occur in the Ni–YSZ cermet. This carbon deposit on the anode surface can obviously block the fuel supply and the transfer of the oxide ions, leading to a decrease in the power efficiency of the cell. Previous published studies highlighted that a

Table 3 Kinetic parameters and equilibrium constants [7, 12–14, 17]

	k^+_{Ei}	K_{Ei}
Methane steam reforming in the cermet	$k^+_{E1} = 1.40 \times 10^5\ T^2 \exp\left(-\frac{27063}{T}\right)$	$K_{E1} = 1.198 \times 10^{23} \exp\left(-\frac{26830}{T}\right)$
Water gas shift reaction	$k^+_{E2} = 1.20 \times T^2 \exp\left(-\frac{12509}{T}\right)$	$K_{E2} = 1.767 \times 10^{-2} \exp\left(-\frac{4400}{T}\right)$
Methane steam reforming in the catalyst layer (Ir)	$k^+_{E4} = 4.77 \times 10^9 \exp\left(-\frac{112047}{RT}\right)$	

Table 4 Material properties at 1,173 K

	Ni–YSZ	YSZ	Ir/CeO_2	LSM–YSZ	Interconnect (×2)
ε (–)	0.40	0.001	0.3	0.40	0.50
λ_B (W m^{-1} K^{-1}) [23]	11.0	2.70	12	6.00	61.0
κ (m^2)	$4.00 \cdot 10^{-15}$	$9.3 \cdot 10^{-22}$	$4.00 \cdot 10^{-15}$	$5.00 \cdot 10^{-15}$	$1.00 \cdot 10^{-11}$
σ_S (S m^{-1}) [24]	0.46[a]	5.13	–	0.62[a]	–
σ_M (S m^{-1})	$6.00 \cdot 10^4$ [25]	–	–	$1.30 \cdot 10^4$ [26]	$1.56 \cdot 10^7$
d_{pore} (m)	$1.00 \cdot 10^{-6}$	$1.00 \cdot 10^{-8}$	$1.00 \cdot 10^{-6}$	$1.00 \cdot 10^{-6}$	$1.00 \cdot 10^{-4}$
τ (–)	4.00		4.00	3.00	1.50

[a] Effective ionic conductivity of the porous electrode

Table 5 Anode gas mixture composition

	RID	GIR
Methane mass fraction	0.296	0.2168
Water mass fraction	0.333	0.024
Argon mass fraction	0.3703	0.7539

catalyst layer thickness equal to 1 mm seems reasonable to avoid carbon deposition into the cermet anode [5, 8].

For simulation, a mixture of fuel and steam is injected at the anode (Table 5) side and air is fed at the cathode. The different molar ratios x_{H_20}/x_{CH_4} that are used at the anode are equal to 1 in DIR or 0.1 in GIR. The value of 0.1 constitutes the arbitrary boundary between GIR and DIR operation. The effect of the steam to methane ratio was performed by varying the S/C from 1 down to 0.01 [4]. Results confirms that the GIR process is very promising for thermodynamic reasons. The fuel flow at the anode is 2.10^{-6} kg s^{-1}. The air flow at the cathode is sufficiently high (10^{-4} kg s^{-1}) so that the molar fraction of oxygen at the cathode side varies only slightly. Finally a temperature of 1,173 K is set for the injected gases. Such processing conditions were imposed to avoid the limitation due to the oxygen reduction at the cathode by a significant reduction in the oxygen concentration along the cell.

3.1 Electrochemical behavior in GIR

The polarization curve (Fig. 2) allows the prediction of the electrochemical performances of the SOFC under DIR and GIR operations with the catalytic layer. Accordingly to thermodynamic point of view, the open cell voltage is higher in GIR mode, in view of the lower steam to methane ratio, which results in higher OCV and thus higher power density. In GIR mode, the quantity of steam produced by the electrochemical reaction is thus sufficient to feed the reforming reaction. However, the cell performance remains rather poor when considering electrolyte-supported cell configuration.

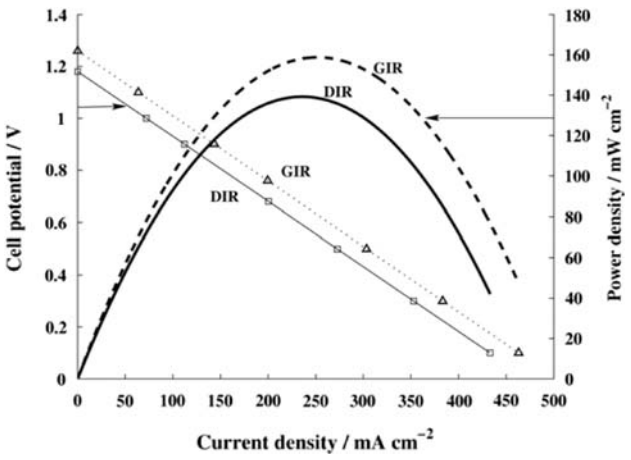

Fig. 2 Calculated polarization curves for various S/C ratios. *Open square* DIR ($x_{H_20}/x_{CH_4} = 1$) and *open triangle* GIR ($x_{H_20}/x_{CH_4} = 0.1$)

For cell potential set to 0.75 V, a current density close to 200 mA cm^{-2} is recorded in GIR mode. Figure 3 presents the ionic ohmic losses in the thick electrolyte. For this operation point, ionic ohmic drop about to 380 mV is recorded. In agreement with the polarization curve (Fig. 2), the ohmic losses in the electrolyte represent nearly 75% of the total losses when considering this cell configuration.

Figure 4 shows the anode overpotentials. As it can be seen on Fig. 4, overpotentials are very weak in the cermet Ni–YSZ even if largest anode overpotential is observed closed to the inlet part of the cell due to the very low hydrogen concentration in GIR mode. This is in agreement with the works of Eguchi et al. [27] on Ni–YSZ cermet.

It results from this first part that the determining steps, in terms of performances, are not related to the electrochemical reaction at the anodic side when a thick electrolyte is used. The major part of the limitations is thus related to the ionic ohmic losses in the thick electrolyte. In the next section the influence of the electrolyte thickness is then investigated.

3.2 Effect of the electrolyte thickness in GIR mode

In this second section the effect of electrolyte thickness is studied by varying the electrolyte from 1 mm down to 50 μm. All other model parameters are kept constant.

The polarization curves (Fig. 5) allow the comparison of the electrochemical performances of the SOFC under GIR mode with thin and thick electrolyte. As expected, the electrochemical performances are much better with a thin electrolyte than with a thick one. For a cell potential set to 0.75 V, the current density is three time larger and a limiting current density is then observed in this case for a thin electrolyte. A sharp decrease of the electrochemical performances appears at high current density as shown by Barnett and co-workers [28].

Figure 6 presents the distribution of the hydrogen partial pressure along the anode for a ratio $x_{H_20}/x_{CH_4} = 0.1$ in GIR in the two cases: thick and thin electrolyte. Figure 6 shows two kinds of propagation for hydrogen and water: convection in the fuel channel and diffusion through the catalyst layer. In the both case, the hydrogen partial pressure is increasing over the length of the cell considered. Since the electrochemical reaction takes place simultaneously, we can say that hydrogen is produced in a largely sufficient way by the involved chemical reactions.

Figure 6a and b also show the evolution of the hydrogen partial pressure as a function of the anodic side thickness. As expected, the most important part of catalytic reforming

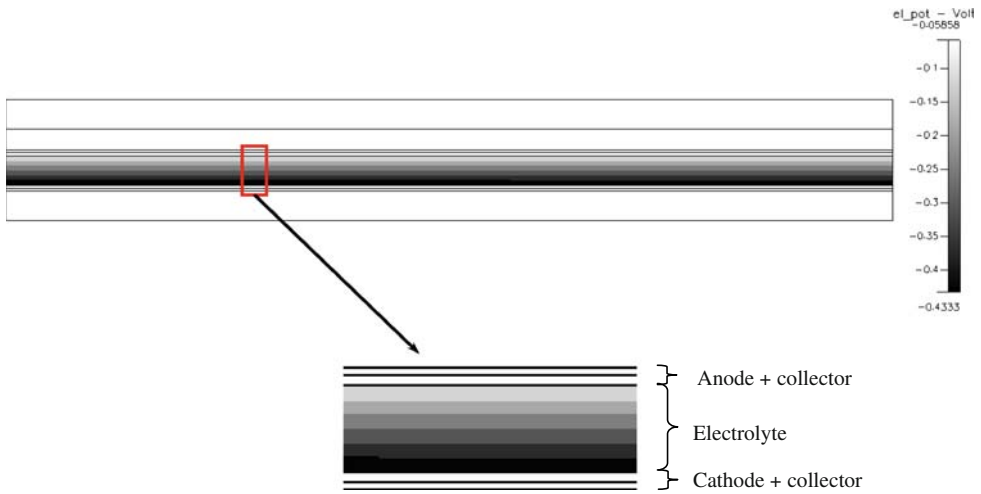

Fig. 3 Ionic ohmic losses in the electrolyte in GIR $(x_{H_2O}/x_{CH_4} = 0.1)$ – $U_{cell} = 0.75$ V and $i = 200$ mA cm^{-2}

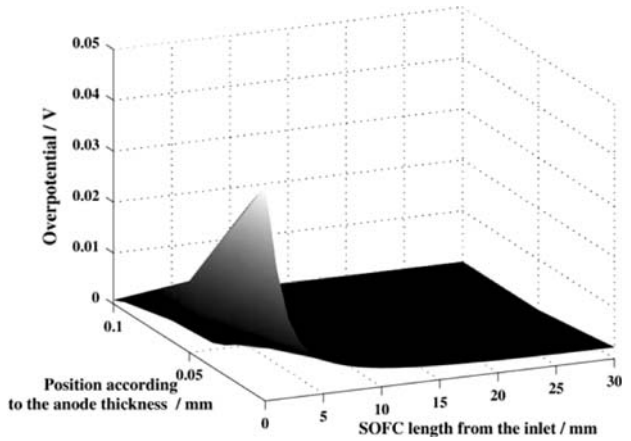

Fig. 4 Anode overpotentials in GIR $(x_{H_2O}/x_{CH_4} = 0.1)$– $U_{cell} = 0.75$ V and $i = 200$ mA cm^{-2}

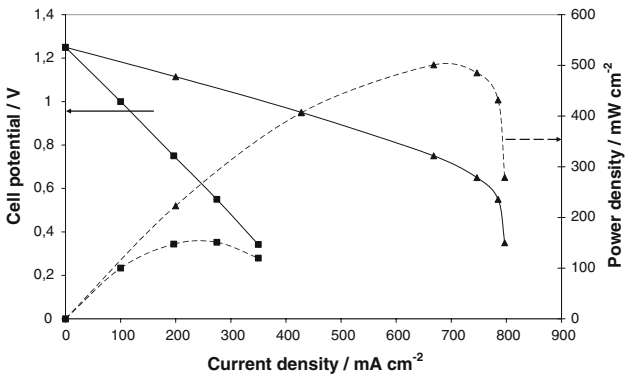

Fig. 5 Polarization curve for two electrolyte thickness in GIR $(x_{H_2O}/x_{CH_4} = 0.1)$. *Filled triangle* $th_{electro} = 0.05$ mm, *filled square* $th_{electro} = 1$ mm

reaction taking place only within the catalyst layer. An increase of the hydrogen partial pressure from the layer–gas interface can initially be observed. Then a decrease of this partial pressure is observed, close to the electrolyte, due to electrochemical consumption in the both case. Nevertheless, strongest hydrogen partial pressure gradient are observed when considering a thin electrolyte (Fig. 6b). This hydrogen depletion can be related to the larger current density when thinner electrolyte layer is used.

Figure 7 presents the distribution of steam partial pressures along the anode in GIR mode with a thin electrolyte. It is worth to notice that important partial pressure gradients through the catalyst layer can be related to the steam clogging at the anodic side. This involves difficulties for hydrogen diffusion making concentration overpotentials strongly increase. At high current density, slow diffusion in the catalyst layer can be responsible for hydrogen depletion when water clogging occurs. It is worth mentioning that methane partial pressure distribution shows two kinds of propagation: convection in the fuel channel and diffusion through the catalyst layer. A methane partial pressure drop is observed along the cell length and toward the catalytic layer, owing to the methane steam reforming reaction (5). Under conditions of GIR (S/C = 0.1), the average S/C ratio into the catalyst layer and cermet increases along the cell length due to the larger steam production through the electrochemical oxidation of hydrogen in the cermet compared to steam consumption in the reforming process.

The evolution of the average overpotential at the anode/electrolyte interface versus the current density (Fig. 8) could be an explanation of this phenomenon. Even though diffusion limitation is generally assumed to be negligible with regard to ionic ohmic drop for an electrolyte-supported SOFC cell, very large anodic overpotentials can be observed at high current density when a thinner electrolyte is considered. This behaviour is clearly due to the large hydrogen depletion through the catalyst and anode thicknesses.

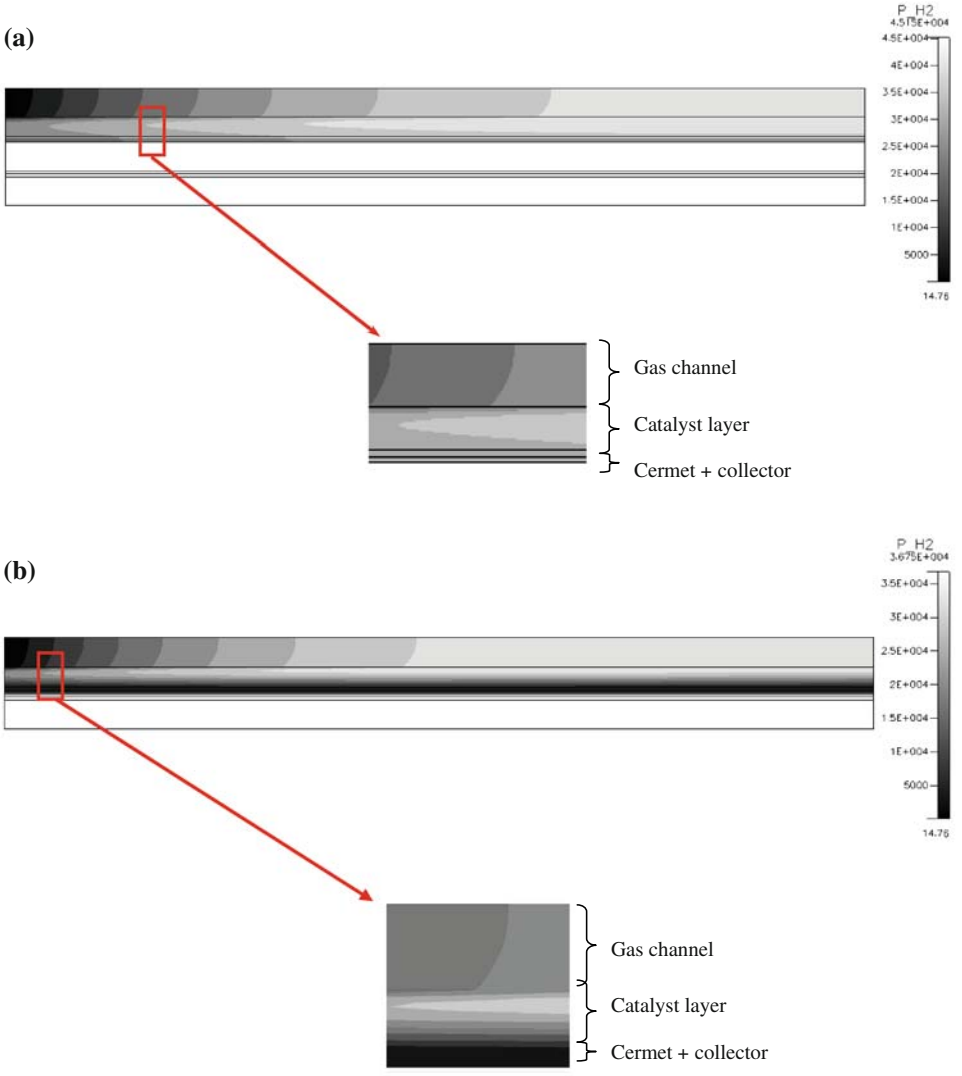

Fig. 6 Hydrogen partial pressure (Pa) in GIR for $x_{H_2O}/x_{CH_4} = 0.1$ for a cell potential $U_{cell} = 0.75$ V: **a** thick electrolyte and **b** thin electrolyte

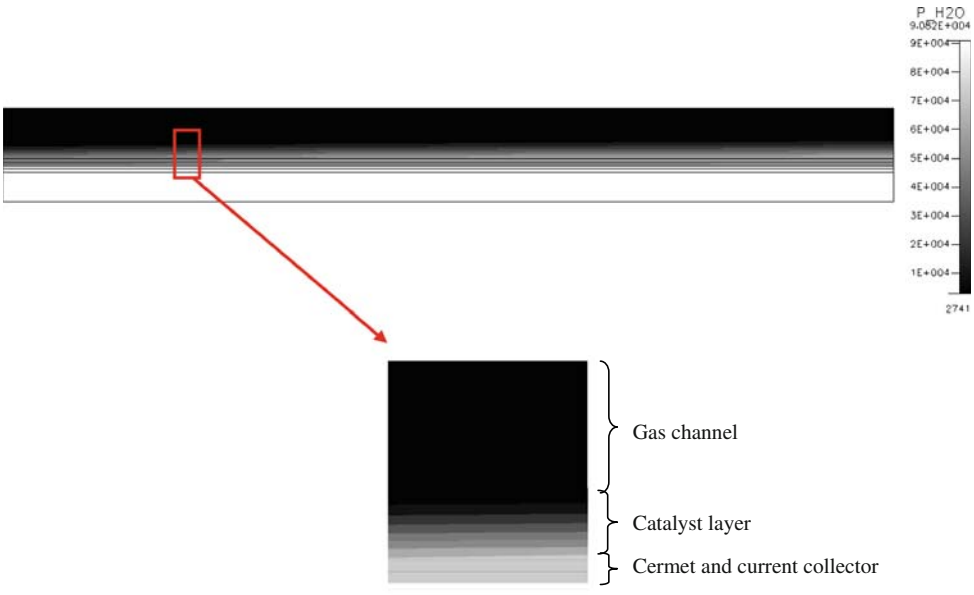

Fig. 7 Steam partial pressure (Pa) in GIR for $x_{H_2O}/x_{CH_4} = 0.1$ for a cell potential $U_{cell} = 0.75$ V: thin electrolyte

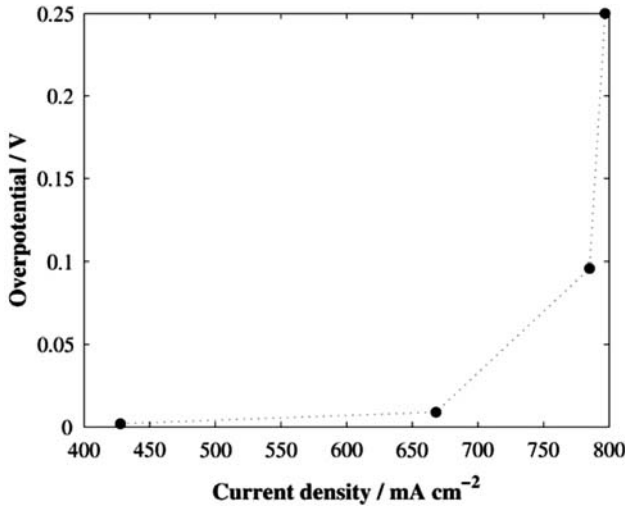

Fig. 8 Overpotential evolution versus current density in GIR for $x_{H_2O}/x_{CH_4} = 0.1$ for a thin electrolyte

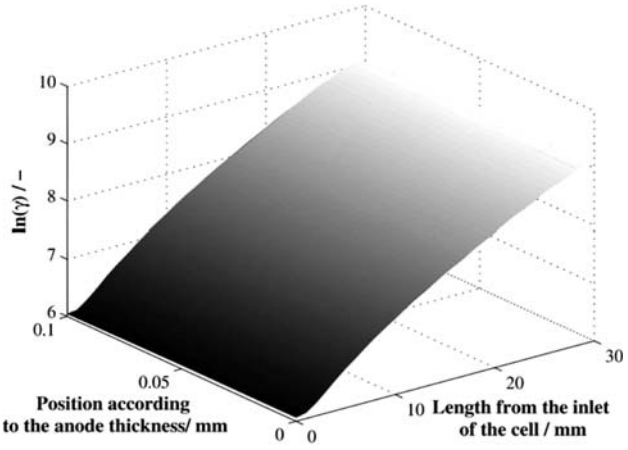

Fig. 10 γ Distribution all over the anode in GIR for $x_{H_2O}/x_{CH_4} = 0.1$ for a cell potential $U_{cell} = 0.75$ V: thin electrolyte

Finally, Fig. 9 presents the temperature variations at the anode side in GIR. For a thin (Fig. 9) or a thick [4] electrolyte, the temperature increase is due to the exothermic hydrogen oxidation. Temperature behaviour in GIR is related to the delocalisation of the reforming reaction and the disappearance of the cooling effect.

Finally, carbon formation is a serious problem in SOFCs that use methane at high temperatures in GIR mode. The Boudouard reaction and the cracking reaction are the major pathways for carbon formation at high operating temperatures [29]. Carbon deposit is then investigated based on a thermodynamic analysis when methane-fuelled SOFCs in the Ni–YSZ cermet (see Annex).

Figure 10 presents the distribution of ln(γ) along the cell length for a current density of 416 mA cm^{-2}. As predicted the risks of carbon deposition are weaker than previously in the case of a thicker electrolyte [5]. Carbon formation is never thermodynamically favoured ($\gamma > 1$) all over the cell. This positive effect is related to the larger water production by the hydrogen oxidation reaction (Eq. 7) when decreasing the electrolyte thickness. Indeed it seems that the higher the current density the better is the protection of cermet against carbon deposit [4].

4 Conclusion

A model using the CFD-Ace software package has been developed for GIR at the anode of a SOFC. It was demonstrated that GIR of methane, using pure methane and in the presence of small quantities of steam, can be achieved without any carbon deposition (from a thermodynamic point of view) using an original geometry including a catalyst layer that promotes methane reforming. The influence of the electrolyte thickness has been investigated by considering the case of a thick or thin electrolyte in this study. As expected, thin electrolyte SOFC cells exhibit larger current density without coking. However a sharp decrease in the electrochemical

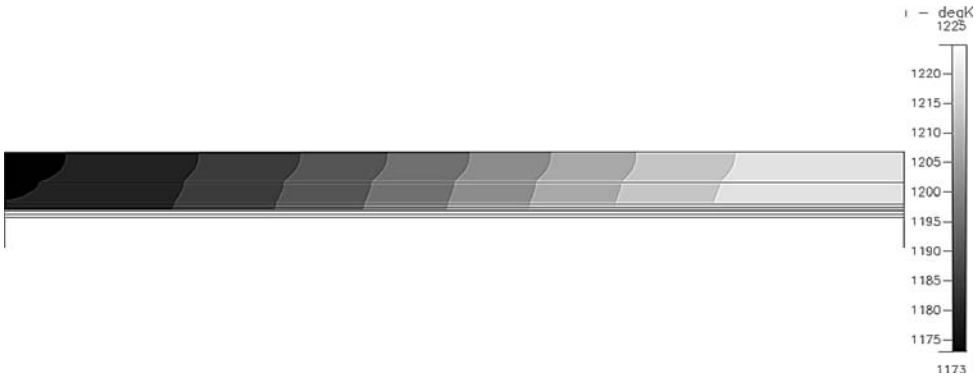

Fig. 9 Temperature distribution all over the anode in GIR for $x_{H_2O}/x_{CH_4} = 0.1$ for a cell potential $U_{cell} = 0.75$ V: thin electrolyte

performances can be observed for high current densities due to steam clogging.

Annex: Thermodynamic analysis of carbon deposition

Carbon deposition is investigated based on a thermodynamic analysis when methane-fuelled SOFCs in the Ni–YSZ cermet; The results will be discussed based on the values of driving forces for carbon deposition [4], defined as the ratios α and β, which depend on the respective reaction quotients and on the equilibrium constants K_B and K_C of the Boudouard and cracking reactions [4, 17], which are temperature functions are:

$$\alpha = \frac{Q_B}{K_B} = \frac{a_{CO_2} a_C}{a_{CO}^2 K_B} \tag{27}$$

$$\alpha = \frac{Q_C}{K_C} = \frac{a_{H_2}^2 a_C}{a_{CH_4} K_C} \tag{28}$$

Q_B and Q_C are the reaction quotients of the Boudouard and cracking reactions, respectively. a_c represents carbon activity and will be taken as 1 in the calculations. Finally a_i is the activity of each gas species I, where P_i is the partial pressure of I and P° is the pressure corresponding to the standard state of i. The unit activity for carbon is considered for any form of deposited solid carbon (carbidic, graphitic…).

For each reaction, if α or $\beta < 1$, the system is not at equilibrium and the reaction will progress towards the right-hand side. In this case, carbon deposition is favored thermodynamically. Equilibrium is reached when α or $\beta = 1$. However, for α or $\beta > 1$, carbon formation is thermodynamically impossible and the reaction will progress towards the left-hand side. After these preliminary considerations, it would appear to be of great interest to investigate the simultaneous influences of both reactions through coefficient γ (Eq. 29), which is explained in the works of Klein et al. [4]:

$$\gamma = \alpha \times \beta \tag{29}$$

References

1. McIntosh S, Gorte RJ (2004) Chem Rev 104:4845
2. Vernoux P, Guindet J, Kleitz M (1998) J Electrochem Soc 145(10):3487
3. Georges S, Parrour G, Hénault M, Fouletier J (2006) Solid State Ion 177:2109
4. Klein J-M, Bultel Y, Georges S, Pons M (2007) Chem Eng Sci 62:1636
5. Klein J-M, Georges S, Bultel Y (2008) J Electrochem Soc 155(4):B333
6. Zhan Z, Barnett SA (2005) Science 308:844
7. Klein J-M (2008) PhD thesis, G INP
8. Klein J-M, Henault M, Roux C, Bultel Y, Georges S (2009) J Power Sources 193:331
9. Mazumder S, Cole JV (2003) J Electrochem Soc 150(11):A1503
10. Bird RB, Byron R, Stewart WE, Lightfoot EN (1960) Transport phenomena. Wiley, New York
11. Divisek J, Mosig J, Steffen B, Stimming U (1994) In: Lapicque F, Storck A, Wragg AA (eds) Electrochemical engineering and energy, proceeding of the third european symposium on electrical engineering. Plenum Press, New York, pp 187–195
12. Xu J, Froment GF (1989) AIChE J 35:88
13. Drescher I, Lehnert W, Meusinger J (1998) Electrochim Acta 43:3059
14. Lehnert W, Meusinger J, Thom F (2000) J Power Sources 87:57
15. Ahmed K, Foger K (2000) Catal Today 63:479
16. Wang Y, Yoshiba F, Kawase M, Watanabee T (2009) Int J Hydrogen Energy 34:3885
17. Hou K, Hughes R (2001) Chem Eng J 82:311
18. Newman J, Thomas-Ayela KE (2004) Electrochemical systems, 3rd edn. Wiley, New York
19. Deseure J, Bultel Y, Dessemond L, Siebert E (2005) Electrochim Acta 50:2037
20. Bruggemann DAG (1935) Ann Phys 24:636
21. Suwanwarangkul R, Croiset E, Pritzker MD, Fowler MW, Douglas PL, Entchev E (2006) J Power Sources 154:74
22. Klein J-M, Bultel Y, Pons M, Ozil P (2008) J Appl Electrochem 38:497
23. Li PW, Suzuki (2004) J Electrochem Soc 151(4):A548
24. Aguiar P, Adjiman CS, Brandon NP (2004) J Power Sources 138:120
25. Simwonis D, Tietz F, Stöver D (2000) Solid State Ion 132:241
26. Costamagna P, Costa P, Arato E (1998) Electrochim Acta 43:967
27. Eguchi K, Setoguchi T, Sawano M, Tamura S, Arai H (1991) In: Singhal, Iwahara (eds) Proceedings of the second international symposium on SOFC, Pennington, p 603
28. Zhan Z, Barnett SA (2005) Solid State Ion 176:871
29. Amor JN (1999) Appl Catal A 176:159